Received: August 27, 2022. Revised: November 1, 2022. 14

INASS

International Journal of
Intelligent Engineering & Systems

http://www.inass.org/

HSIS-Net: Hyperspectral Image Segmentation Using Multi-view Active Learning Based FCSN

Mantena Krishna Satya Varma[1]* **Raja Kulasekaran[1]** **Nynalasetti Konadala Kameswara Rao[2]**

[1]*Department of Information Technology, Annamalai University, Chidambaram, Tamil Nadu, India*
[2]*Department of Computer Science and Engineering, Sagi Ramakrishnam Raju Engineering, Bhimavaram, Andhra Pradesh, India*
* Corresponding author's Email: mkrishnasvarma@gmail.com

Abstract: Hyperspectral image (HSI) segmentation and classification is trending research in military and civil applications area. However, HSI classification is facing various challenges in analyzing spectral and spatial regions. In order to improve the performance of HSI classification models, segmentation is essential step. Therefore, this article is focused on implementation of unified HSI segmentation network (HSIS-Net) using active learning. Initially, HSI preprocessing operation is performed to normalize the spectral-spatial regions. Then, joint spatial-spectral boundary extraction operation is performed using spatial information divergence (SID) and spectral correlation mapper (SCM). Finally, segmentation of boundary estimated HSI bands is performed using multi-view active learning network based fully convolutional segmentation network (MAL-FCSN). The simulations revealed that the proposed HSIS-Net resulted in superior segmentation performance with segmentation accuracy (SA) of 0.999, and segmentation F1-score of 0.999 as compared to the existing HSI classification approaches for four publicly available HSI datasets.

Keywords: Hyperspectral image, Fully convolutional segmentation network, Spatial information divergence, Multi-view active learning network.

1. Introduction

Optical images are the prime sources of information in remote sensing data analysis. Since their inception, they have played a vital role in the success of various information mining and image interpretation tasks since their inception [1]. Contemporary examples include, but are not limited to, mapping (or classification) and monitoring applications of land use/land cover change [2], health care, weather, and climate forecasts [3], and Planetary exploration missions [4]. Imaging systems use sensors, which are sensitive to one or more wavelengths of an electromagnetic spectrum, to capture images for the visual representation of an area. Depending on the imaging techniques used, the visual representation and structure of an image can take many forms to convey different levels of information of the desired scanning scene based on the surface reflectance. Some optical imaging techniques used in modern times include panchromatic imaging, red, green, and blue (RGB) imaging [5], HSI, thermal imaging, etc. HSI remote sensing combines two technologies, namely imaging and spectroscopy [6]. HSI for remote sensing can be divided into two main techniques based on the continuity of the data stored in the wavelength domain, and multispectral-HSI [7].

In the past few years, HSI systems have gained significant attention from researchers across various scientific and engineering disciplines [8]. Unlike traditional panchromatic and RGB imaging systems, HSI systems use specialized sensors operating primarily from the visible through infrared wavelength ranges to acquire images with more than three spectral bands [9]. Further, HSI is the technique of producing images containing both spatial and spectral domain information of scanning area on the surface of the earth based on surface reflectance [10]. The HSIs are three-dimensional data structures having two spatial dimensions and one spectral

dimension. The main difference between normal images and HSI is in the usage of the sampling technique, the bandwidth of each spectral channel, and the number of bands [11]. Multispectral remote sensing collects MSI data that have several bands each sampled at discrete, often discontinuous, wavelengths with wider spectral bandwidths, i.e., low spectral resolution. While hyperspectral remote sensing collects HSI data having spectral bands, each sampled at contiguous wavelengths with narrow bandwidths (typically in 10nm or less), i.e., high spectral resolution [12]. The evolution of very high-resolution HSIs classification has proved to be particularly advantageous for most remote sensing image interpretation tasks. But there are challenges associated with the use of HSIs for transforming [13] the rich spectral data into information for applications. Whereas with HSIs, class separability is largely owing to the high spectral resolution. However, the increase in the dimensionality of the data increases the possibility of problems with the curse of dimensionality. In practice, it is difficult or not possible to collect complete information about the training samples of classes of interest. Only a limited number of labeled samples of classes of interest are only available at hand before training.

Therefore, to overcome these challenges, the novel contribution of this work is organized as follows:

- HSI image is divided into multiple spectral bands, and preprocessing, boundary analysis and segmentation operation is carried out on each band.
- Spatial boundaries are extracted using SID and spectral boundaries are extracted using SCM.
- Multi-layer perception-based MAL-FCSN is used to perform the segmentation operation by analyzing the sub-pixel, pixel and super-pixel views of various regions.

Rest of the article is organized as follows: section 2 deals with the related work, section 3 delas with the proposed HSIS-Net implementation analysis, section 4 deals with the results and discussions, and section 5 delas with the conclusion.

2. Related work

This section performs the detailed survey on segmentation approaches. There are three different categories of segmentation approaches are used, pixel-level segmentation [15], object-level segmentation [16], and sub-pixel segmentation or unmixing [17]. The choice of approach depends mainly on the application requirement since they offer both advantages and limitations. Time-critical and real-time applications such as target detection, diurnal change detection, industrial quality inspection require real or near real-time computation solutions and segmentation framework. In particular, there are a plethora of applications, which bank upon HSIs, needing real-time processing systems for image analysis. There are different types of dee-learning depending upon the network architecture used to perform the HSI segmentation tasks, some of the deep learning models are recurrent neural networks [18], cyclic neural network, convolutional neural networks, and deep belief neural networks. However, deep learning convolution neural networks (DLCNN) [19] have attracted widespread attention in many vital applications.

In [20] authors implemented the object-based image analysis (OBIA) model for HSI segmentation. In contrast to grayscale and color images, HSIs provide the benefit of analyzing images in a pixel-by-pixel fashion accurately using spectral information alone. Further, A semi-supervised reduced-space (SSRS) method [21] is implemented for HSI segmentation. This method benefit is due to the increasing order of pixel-wise spectral information from panchromatic. In [22] authors implemented the conditional random field (CRF) for HSI segmentation. The most common limiting factors known to increase the risk in analyzing HSIs [23]. Due to the low spectral resolution, the separability of classes of interest (within classes and between classes) is limited. In [24] authors implemented the end-to-end fully convolutional network (EFCN) for HSI segmentation. Then, recurrent convolutional neural network (RCNN) is used to perform the segmentation operation. In [25] authors implemented a hybrid network, which contains principal component analysis (PCA) based feature extraction, spectrally segmented-folded-PCA (SSeg-Fol-PCA) for HSI segmentation, support vector machine (SVM)-based segmentation. In [26] authors implemented the entropy rate super-pixel (ERS) approach for HSI segmentation, multi-spectral ERS approach is used for joint spatial-spectral feature analysis. Further, two-branch convolutional neural network (TBNN) is used to perform the segmentation. However, this method suffering with high computational complexity. The adaptive spatial pyramid constraint network (ASPCN) [27] is used to perform the HSI segmentation, which utilizes limited training samples. Here, dimensionality reduction refers to the process of reducing the number of attributes or features either by using feature selection or by feature extraction methods. In [28] authors implemented the HyperUnet model for HSI

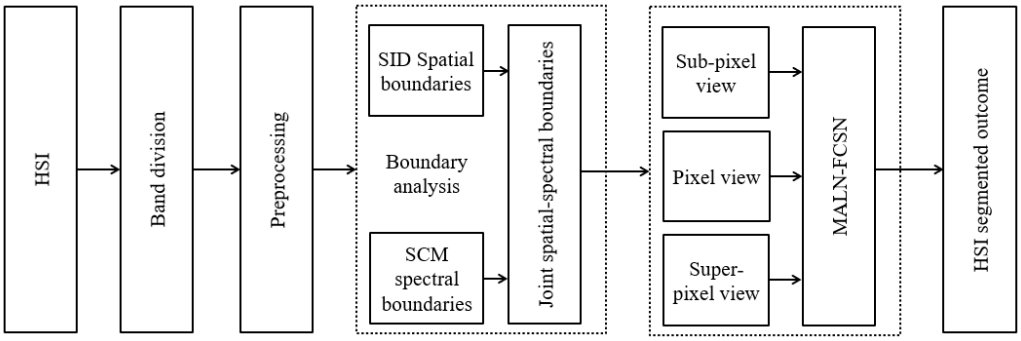

Figure. 1 Proposed HSIS-Net architecture

segmentation. A typical objective of HSI processing and analysis in different fields of application includes one or more of the techniques such as dimensionality reduction, target detection, and segmentation. In [29] authors implemented the covariance matrix representation (CMR) model for spectral–spatial feature extraction using locally homogeneous properties. This prominence is because the segmentation technique helps transform the large volumes of remotely sensed image data into useful information with multiple usages.

In [30] authors implemented the spatial and spectral kernels generation network (SSKNet) for HSI segmentation using spatial and spectral kernels generation. In [31] authors implemented the spectral–spatial based SuperPCA approach for HSI feature extraction and segmentation operation is carried out using SVM. In [32] authors implemented the multiscale curvature filters-for HSI feature extraction. Due to the stochastic nature of landscapes, there are different types of uncertainties ranging from image acquisition to image processing and analysis [33], including training and segmentation. Some of the uncertainties are sensor noise, limited training knowledge of known classes. The incomplete knowledge about the actual number of classes in the imagery, i.e., presence of unknown classes, which are unknown or unseen during training [34]. The uncertainties are one of the significant factors responsible for omission and commission errors.

3. Proposed methodology

The conventional HSI segmentation models are facing the challenges with complexities, noises, errors, and uncertainties. Further, challenges are inducing by these methods during adoption in applications, which slows down the application performance. Therefore, the development of novel algorithms is needed to exploit the full latent potential of spatial-spectral information present in HSIs. Fig. 1 shows the block diagram of proposed HSIS-Net. Initially, HSI Processing operation is performed for normalizing the spatial-spectral bands of HSI, which also removes the different types of noises and enhances the region. In addition, spatial boundaries are extracted using SID, spectral boundaries are extracted using SCM methods and joint spatial-spectral boundary map is formed by concatenation. Finally, multi-layer perception adopted transfer learning-based MAL-FCSN is used to perform the segmentation operation, which spates the spatial-spectral regions based on boundary analysis.

3.1 Data processing

Let us consider a 3D HSI data cube denoted by $X \in \mathbb{R}^{m \times n \times d}$ has m rows or lines, n columns or samples, and d spectral bands or dimensionality. For convenience, the 3D data cube X of size $m \times n \times d$ can be written into a 2D $\times$ N (where $N = m \times n$) matrix form ($X \in \mathbb{R}^{d \times N}$), known as data matrix as shown in Eq. (1). The data matrix $\boldsymbol{X}$, is typically defined as the rastered ordering of N column pixel vectors $x_i \in \mathbb{R}^d$, such that $X = [x_1, x_2, \ldots \ldots x_N] \in \mathbb{R}^{d \times N}$. Where each pixel vector x_i, see Eq. (2), represents a spectral measurement and N is the total number of pixel vectors, i.e., N is product of m and n,

$$X = [x_1, x_2, \ldots \ldots x_N]_{dxN} = \begin{bmatrix} x_{11} & \cdots & x_{N1} \\ \vdots & \ddots & \vdots \\ x_{1d} & \cdots & x_{Nd} \end{bmatrix} = X \in \mathbb{R}^{d \times N} \quad (1)$$

$$x_i = \begin{bmatrix} x_{i1} \\ x_{i2} \\ \vdots \\ x_{id} \end{bmatrix} \in \mathbb{R}^d \quad (2)$$

For a pixel-by-pixel-based image analysis, each dimensional pixel vector is given as input to the algorithm as one-by-one in a streaming fashion. For instance, assume that the HSI arrives in a pixel-by-pixel manner from a data matrix or in band-interleaved-by pixel format from a sensor. As a result, a pixel vector-based analysis can be performed. In

other two image data formats, such as band-interleaved-by-line and band sequential, the 3D data cube is transformed to a 2D data matrix and then streamed pixel-wise to the segmentation algorithm. Further, noise removal operation is carried out, which enhances the pixel wise information.

3.2 Boundary extraction

The HSI images consist of both spatial and spectral boundaries, where spatial boundaries hold the temporal redundancy and spectral boundaries holds the structural boundaries. These are the edge oriented statistical properties, which holds the spatial and spectral information of HSI. Therefore, the extraction of boundaries should be done carefully without losing the original information. Here, spatial boundaries (ψ_{SID}) are extracted using SID, spectral boundaries (ψ_{SCM}) are extracted using SCM methods and joint spatial-spectral boundary map is formed by concatenation.

3.2.1. SID

SID is a stochastic measure derived from information theory. It is used for measuring spatial similarity and discriminability between unknown test pixel spatial and target reference spatial. SID views each pixel vector as a random variable and calculates the probabilistic behaviors between the reference pixel vector x and test pixel vector z. The probability vectors of x and z are given by $p = \{p_i\}_{i=1}^{d}$ and $q = \{q_i\}_{i=1}^{d}$, respectively, where p_i and q_i are given as follows:

$$p_i = \frac{x_i}{\sum_{k=1}^{d} x_k} \tag{3}$$

$$q_i = \frac{z_i}{\sum_{k=1}^{d} x_k} \tag{4}$$

The SID ($(\psi_{SID}$) between x and z is given by

$$(\psi_{SID}(z, x_i) = D(x_i || z) + D(z || x_i \ \ ) \tag{5}$$

$$D(x_i || z) = \sum_{l=1}^{d} p_l D_l(x_i || z) = \sum_{l=1}^{d} p_l \log_2 \left(\frac{p_i}{q_i}\right) \tag{6}$$

$$D(z || x_i) = \sum_{l=1}^{d} q_l D_l(z || x_i) = \sum_{l=1}^{d} q_l \log_2 \left(\frac{p_i}{q_i}\right) \tag{7}$$

Where $D(x_i \parallel z)$ and $D(z \parallel x_i)$ are relative entropy of x with respect to z and z with respect to x, respectively, and are also known as Kullack-Leibler divergence or cross-entropy. The values of ψ_{SID} ranges from 0 to ∞. A value of $\psi_{SID} = 0$ indicates a perfect match with no divergence between the two spatial. The lower the ψ_{SID} value, the better the level of similarity between the reference spatial and unknown test spatial.

3.2.2. SCM

SCM is a derivative of Pearson's linear correlation coefficient. It is commonly used to measure the similarity between the reference pixel and unknown pixel. The spectral matching performance of SCM is relatively higher than spectral angle mapper (SAM) because SCM can perceive a difference between positive and negative correlation. Unlike SAM, SCM is invariant to the linear transformation of spectra. The mathematical expression of SCM, ψ_{SCM}, for any z is given by

$$\psi_{SCM}\ (z, x) = \frac{\sum_{l=1}^{d} (z_l - \bar{z})\ (x_l -)}{\sqrt[2]{[\sum_{l=1}^{d} (z_l - \bar{z})^2\ ][\sum_{l=1}^{d} (x_l - \bar{x})^2\ ]}} \tag{8}$$

$$\bar{x} = \frac{1}{d}\left(\sum_{l=1}^{d}\ x_l\right) \tag{9}$$

$$\bar{z} = \frac{1}{d}\left(\sum_{l=1}^{d}\ z_l\right) \tag{10}$$

Where $\bar{x}$ and $\bar{z}$ are the means of x and z pixel vectors, respectively. The values of the ψ_{SCM} ranges from − (i.e., no similarity) to + (i.e., perfect similarity).

3.3 MAL-FCSN

Active learning is one of the most widely researched approaches in the image segmentation domain. This is because of its ability to provide accurate predictions for a given training set. Further, the multi-view active learning performs the segmentation by analyzing the sub-pixel, pixel and super- pixel views of various regions. Fig. 2 presents the block diagram of multi-layer perception-based MAL-FCSN segmentation. Fig. 3 shows the layer wise architecture diagram of FCSN model. There are generally two phases or stages involved in using any MAL-FCSN technique, namely the training phase and the testing phase. The key idea in MAL-FCSN can be summarized as the task of learning a mapping function f that maps inputs (x) to a unique segmented label from a prefixed set of discrete outputs labels, categories or target (y).

Mathematically, MAL-FCSN is expressed as $f: x \rightarrow y$ or $y = f(x)$. In the training stage of the MAL-FCSN learning process, a discriminant function f is formulated using a training set

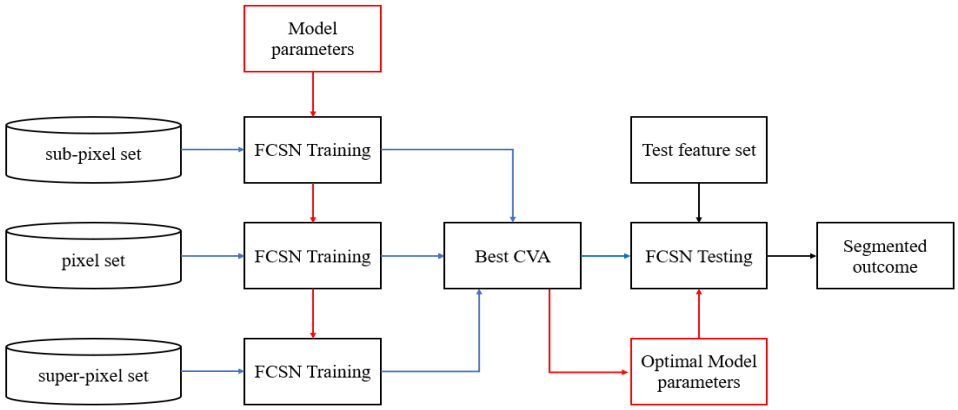

Figure. 2 HSI segmentation using MAL-FCSN

consisting of l labeled pixel vectors, i.e., $S = \{ x_i, y_i \}_{l=1}^{l}$ with training samples $x_i \in \mathbb{R}_d$, and the corresponding class labels $y_i \in \mathbb{R}_l$. To produce a generalized classification model f using S, a grid search method with a cross-validation (CV) strategy is adopted to find the optimal values of model parameters and free parameters. During training, algorithm-specific free parameter $\theta_f = \{\theta_{f_1}, \theta_{f_2}, \ldots\ldots, \theta_{f_i}\}$ are given as input to the training model to produce optimal model parameters $\theta_m = \{\theta_{m_1}, \theta_{m_2}, \ldots, \theta_{m_j}\}$ to make the model fit the data.

The available training data S is then split into three different sample subsets, namely sub-pixel set ($S_{Sub} \subseteq S$), pixel set ($S_{Pixcel} \subseteq S$), and super-pixel set ($S_{super} \subseteq S$). Then, cross validation accuracy (CVA) is calculated for each sub-set by rand sub sampling validation. The optimal combination of model parameters is selected highest values of CVA. The procedure is done for tuning or configure the optimal model parameters (θ_m). In the second phase of the MAL-FCSN approach, the trained model (i.e., $f\ (x: \theta_m)$ is used for segmented label class prediction for each test pixels. Finally, the test features (S_{Test}) are compared with trained data and produces the segmented outcome.

3.3.1. FCSN segmentation

Transfer learning techniques have seen a global trend towards increase in popularity and use across various scientific and engineering disciplines in recent years. The increasing popularity and usage of these algorithms are mainly because of their ability to learn representative and discriminative features hierarchically employing various layers of abstraction. The word transfer learning usually means a depth of more than two hidden layers in a neural network architecture. Fig. 3 shows the FCSN model architecture for segmentation of HSI, which contains the convolutional encoder and decoder networks.

Here, encoding process is used to reduce the number of features using max pooling layers, there by performs the segmentation operation in sub-pixel level with detailed edge identification. After the encoding phase, a decoding procedure using a number of up sampling layers, which is used to perform the increased number of pixels and performs the segmentation operation in super-pixel level. Up sampling is accomplished by the use of transposed convolution (Conv2DTranspose), which is also referred to more precisely as fractionally strided convolution. This is an operation that goes in the opposite direction of a convolution and enables us to translate the activations into something meaningful related to the size of the image by scaling up the activation size to the same size as the image. This is accomplished by scaling the activation size up to the same size as the image. This is performed by increasing the size of the activation to be the same as the size of the picture. Scaling up the activation size to match the image's size does this. A convolution layer produces feature maps using the following expression

$$x_j^l = f\left(\left(\sum_i x_i^{l-1} * k_{ij}^l\right) + b_i^l\right) \qquad (11)$$

Here, x_i^{l-1} is the i^{th} feature map of $(l-1)^{th}$ layer, x_j^l represents the j^{th} feature map of current i^{th} layer, and $f(.)$ is a non-linear activation function. The trainable parameters k_{ij}^l and b_i^l represents the kernel or weights and bias in the convolution layer, respectively. The pooling layer is used to down sample the feature maps using either max or average rule. The fully connected layers stack the reduced features to perform segmentation.

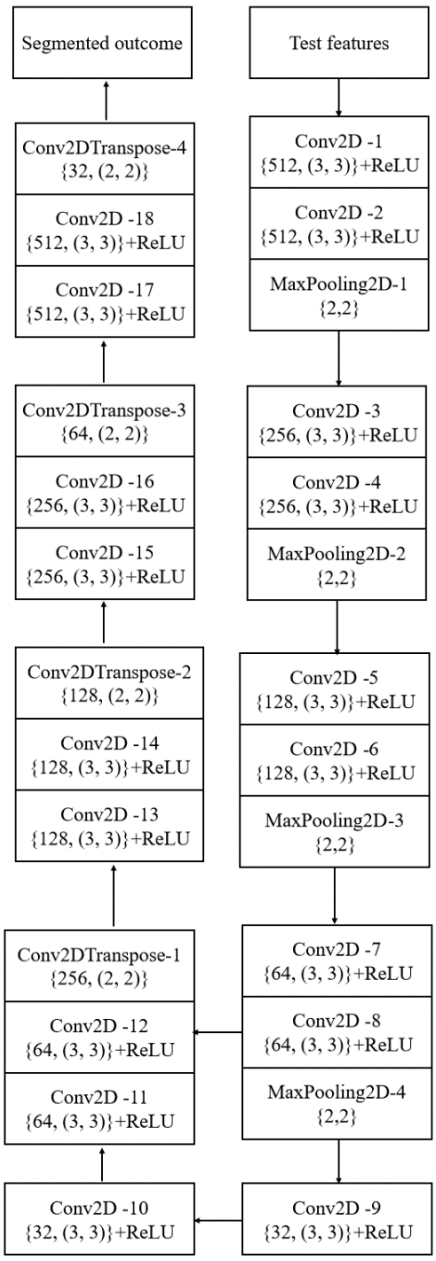

Figure. 3 FCSN architecture

4. Results and discussion

The University of Pavia, Indian Pines, Salinas dataset, and Kennedy space center (KSC) dataset are the four datasets used for the simulations [35]. Each dataset has distinct categories with its own characteristics. As a result, the performance of the suggested system was successfully assessed using several performance indicators for each dataset. Here, segmentation accuracy (SA), segmentation precision (SP), segmentation recall (SR), segmentation F1-score (SF1) are the segmentation performance measures.

4.1 Dataset

Indian Pines: Above the Indian Pines test site in northwest Indiana, the AVIRIS sensor recorded the Indian Pines dataset. Each picture in this collection comprises 145145 pixels and 220 spectral bands with wavelengths ranging from 0.4 to 2.5 m. There are 16 categories in this picture that need to be categorised, such as the grassy field, the trees, and more.

University of Pavia: The ROSIS03 satellite sensor captured this HSI image of the metropolitan region around the University of Pavia. This HSI has 103 spectral bands, and each band picture has a resolution of 610340 pixels with a spectral coverage of 0.43 to 0.86 meters. There are nine categories in

Table 1. Segmentation performance evaluation on the Indian-pines dataset

Metrics	OBIA [20]	CRF [22]	SSRS [21]	EFCN [24]	CRF [23]	SSeg-Fol-PCA [25]	HyperUnet [28]	HSIS-Net
SA	0.548	0.590	0.626	0.706	0.746	0.831	0.882	0.993
SP	0.579	0.686	0.683	0.775	0.810	0.888	0.909	0.987
SR	0.642	0.738	0.792	0.793	0.777	0.869	0.901	0.973
SF1	0.657	0.726	0.722	0.759	0.799	0.823	0.905	0.983

Table 2. Segmentation performance evaluation on the KSC dataset

Metrics	OBIA [20]	CRF [22]	SSRS [21]	EFCN [24]	CRF [23]	SSeg-Fol-PCA [25]	HyperUnet [28]	HSIS-Net
SA	0.561	0.669	0.624	0.786	0.884	0.893	0.920	0.991
SP	0.521	0.679	0.668	0.760	0.810	0.880	0.906	0.997
SR	0.538	0.622	0.674	0.796	0.883	0.892	0.933	0.983
SF1	0.595	0.616	0.683	0.718	0.839	0.867	0.922	0.993

(a) (b) (c)

Figure. 4 The segmentation results of Indian pines dataset:(a) ground truth, (b) boundary detection, and (c) final segmentation

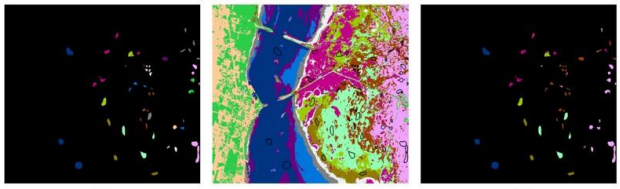

(a) (b) (c)

Figure. 5 The segmentation results of KSC dataset: (a) ground truth, (b) boundary detection, and (c) final segmentation

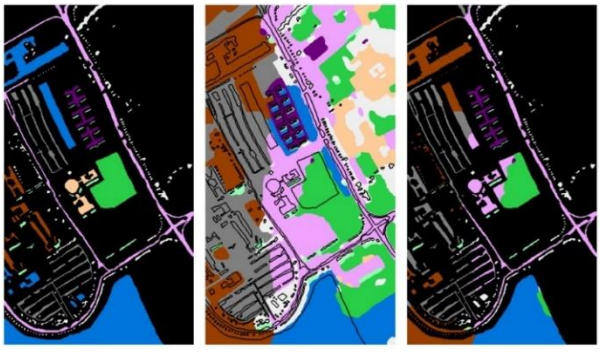

(a) (b) (c)

Figure. 6 The segmentation results of Pavia University dataset: (a) ground truth, (b) boundary detection, and (c) final segmentation

this scenario that need to be categorized, including asphalt, meadows, and other things.

KSC dataset: With wavelengths spanning from 0.4 to 2.5 m, AVIRIS gathered information from the KSC in 224 bands. The water absorption bands are categorized using a total of 176 spectral bands. There are 13 possible land-cover categories in this dataset.

Salinas dataset: Additionally, a Salinas dataset was obtained by the AVIRIS sensor, which had images of the Salinas Valley in California with a spatial resolution of 3.7 meters. This HSI has 220 bands, each of which has a picture with a 512 by 217-pixel resolution.

4.2 Performance evaluation

Fig. 4 shows the segmented outcomes of Indian pines dataset. The joint SID-SCM method accurately identifies segmented outcome of Indian pines dataset and it is matched to ground truth.

Table 1 presents the segmentation performance comparison of various approaches, where proposed HSIS-Net resulted in superior performance as compared existing segmentation methods like OBIA [20], CRF [22], SSRS [21], EFCN [24], CRF [23], SSeg-Fol-PCA [25], and HyperUnet [28].

The KSC is also another important dataset, which contains the greatest number of pixels in the background. Fig. 5 shows that the proposed method results in a much similar segmented outcome as ground truth. Table 2 presents the segmentation performance comparison of various approaches, where proposed HSIS-Net resulted in superior performance as compared existing segmentation methods like OBIA [20], CRF [22], SSRS [21], EFCN [24], CRF [23], SSeg-Fol-PCA [25], and HyperUnet [28].

The Pavia dataset attracts significant attention in the HSI classification process as it contains more robust ground truth and a smaller number of classes. Fig. 6 shows that the proposed method results in a much similar segmented outcome as ground truth.

Table 3. Segmentation performance evaluation on the Pavia University dataset

Metrics	OBIA [20]	CRF [22]	SSRS [21]	EFCN [24]	CRF [23]	SSeg-Fol-PCA [25]	HyperUnet [28]	HSIS-Net
SA	0.542	0.628	0.751	0.816	0.888	0.891	0.927	0.999
SP	0.590	0.686	0.747	0.813	0.879	0.897	0.915	0.989
SR	0.536	0.741	0.766	0.843	0.839	0.928	0.945	0.992
SF1	0.575	0.731	0.784	0.834	0.890	0.914	0.934	0.999

Table 4. Segmentation performance evaluation on the Pavia University dataset

Metrics	OBIA [20]	CRF [22]	SSRS [21]	EFCN [24]	CRF [23]	SSeg-Fol-PCA [25]	HyperUnet [28]	HSIS-Net
SA	0.574	0.796	0.803	0.829	0.870	0.916	0.934	0.999
SP	0.545	0.751	0.810	0.868	0.883	0.913	0.932	0.998
SR	0.591	0.665	0.831	0.832	0.909	0.928	0.966	0.997
SF1	0.620	0.715	0.853	0.883	0.915	0.939	0.942	0.999

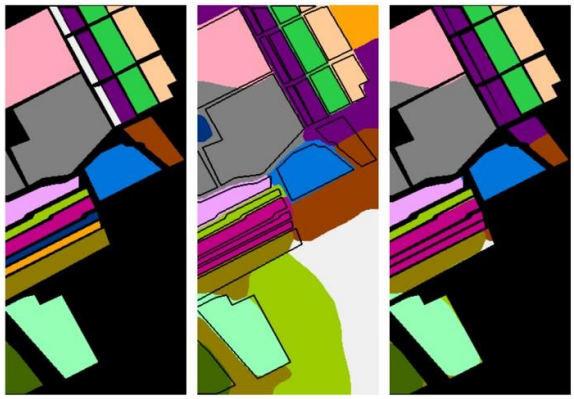

(a) (b) (c)

Figure 7. The segmentation results of Salinas dataset: (a) ground truth, (b) boundary detection, and (c) final segmentation

Table 3 presents the segmentation performance comparison of various approaches, where proposed HSIS-Net resulted in superior performance as compared existing segmentation methods. Fig. 7 shows the segmented outcomes of Salinas dataset. The joint SID-SCM method accurately identifies the segmented outcome of Salinas dataset, and it is matched to ground truth. Table 4 presents the segmentation performance comparison of various approaches, where proposed HSIS-Net resulted in superior performance as compared existing segmentation methods.

5. Conclusions

This article implemented the HSIS-Net for HSI segmentation using multi-view active learning adopted with transfer learning. Initially, HSI preprocessing operation is carried out for normalization of spatial-spectral bands and also removed the different types of noises. Further, spatial boundaries are extracted using SID, spectral boundaries are extracted using SCM and joint boundary map was formed. Furthermore, multi-layer perception-based MAL-FCSN generates the HSI segmented outcome by analyzing the sub-pixel, pixel and super- pixel views of various regions. Here, transfer learning based FCSN model was used to segment the HSI regions based on spatial-spectral boundary analysis, which contain the multi-layer encoder and decoder networks. This work can be extended with natural inspired optimization algorithms for better segmentation and classification.

Conflicts of interest

The authors declare no conflict of interest.

Author contributions (Mandatory)

"Conceptualization, M. Krishna Satya Varma; methodology, M. Krishna Satya Varma; software, M. Krishna Satya Varma; validation, M. Krishna Satya Varma; formal analysis, M. Krishna Satya Varma; investigation, M. Krishna Satya Varma; writing—original draft preparation, M. Krishna Satya Varma; writing—review and editing, M. Krishna Satya Varma, K. Raja, N. K. Kameswara Rao.

References

[1] P. Ghamisi, J. Plaza, Y. Chen, J. Li, and A. Plaza, "Advanced spectral classifiers for hyperspectral images: A review", *IEEE Geoscience and Remote Sensing Magazine*, Vol. 5, No. 1, pp. 8–32, 2017.

[2] M. H. Phan, S. L. Phung, K. Luu, and A. Bouzerdoum, "Efficient Hyperspectral Image Segmentation for Biosecurity Scanning Using Knowledge Distillation from Multi-head Teacher", *Neurocomputing*, Vol. 504, pp. 189-203, 2022.

[3] L. Zhang, L. Zhang, D. Tao, X. Huang, and B. Du, "Hyperspectral remote sensing image target

detection based on supervised metric learning", *IEEE Transactions on Geoscience and Remote Sensing*, Vol. 52, No. 8, pp. 4955–4965, 2014.

[4] A. Kaul, "A Review of Hyperspectral Image Classification with Various Segmentation Approaches Based on Labelled Samples", *Smys, S., Tavares, J.M.R.S., Balas, V.E. (eds) Computational Vision and Bio-Inspired Computing. Advances in Intelligent Systems and Computing*, Singapore, Vol. 1420, 2022.

[5] S. L. Polk, K. Cui, R. J. Plemmons and J. M. Murphy, "Active Diffusion and VCA-Assisted Image Segmentation of Hyperspectral Images", *IEEE International Geoscience and Remote Sensing Symposium*, pp. 1364-1367, 2022.

[6] J. C. Cohrs, C. Bajaj, and B. Berkels, "A distribution-dependent Mumford-Shah model for unsupervised hyperspectral image segmentation", *arXiv:2203.15058*, 2022.

[7] B. Manifold, S. Men, R. Hu, and D. Fu, "A versatile deep learning architecture for classification and label-free prediction of hyperspectral images", *Nature Machine Intelligence*, Vol. 3, No. 4, pp. 306-315, 2021.

[8] X. Liu, J. Yu, T. Kurihara, L. Xu, Z. Niu, and S. Zhan, "Hyperspectral imaging for green pepper segmentation using a complex-valued neural network", *Optik*, Vol. 265, Article ID 169527, 2022.

[9] L. Wei, M. Yu, Y. Zhong, J. Zhao, Y. Liang, and X. Hu, "Spatial-spectral fusion based on conditional random fields for the fine classification of crops in UAV-borne hyperspectral remote sensing imagery", *Remote Sensing*, Vol. 11, No. 7, p. 780, Apr. 2019.

[10] S. Subudhi, R. N. Patro, P. K. Biswal and F. Dell'Acqua, "A survey on superpixel segmentation as a preprocessing step in hyperspectral image analysis", *IEEE Journal of Selected Topics in Applied Earth Observations and Remote Sensing*, Vol. 14, pp. 5015-5035, 2021.

[11] S. L. Polk, A. H. Y. Chan, K. Cui, R. J. Plemmons, D. A. Coomes, and J. M. Murphy, "Unsupervised detection of ash dieback disease (Hymenoscyphus fraxineus) using diffusion-based hyperspectral image clustering", *arXiv preprint arXiv:2204.09041*, 2022.

[12] S. R. Delwiche, I. Baek, and M. S. Kim, "Does spatial region of interest (ROI) matter in multispectral and hyperspectral imaging of segmented wheat kernels?", *Biosystems Engineering*, Vol. 212, pp. 106-114, 2021.

[13] H. Du, H. Qi, X. Wang, R. Ramanath, and W. E. Snyder, "Band selection using independent component analysis for hyperspectral image processing", In: *Proc. 32nd Appl. Imagery Pattern Recognit. Workshop*, pp. 93–98, 2003.

[14] J. G. Zaballa, K. Basterretxea, J. Echanobe, M. Martínez, and I. D. Campo, "Exploring Fully Convolutional Networks for the Segmentation of Hyperspectral Imaging Applied to Advanced Driver Assistance Systems", In: *Proc. of International Workshop on Design and Architecture for Signal and Image Processing*, Springer, Cham, pp. 136-148.

[15] G. Jaiswal, A. Sharma, and S. K. Yadav, "Critical insights into modern hyperspectral image applications through deep learning", *Wiley Interdisciplinary Reviews: Data Mining and Knowledge Discovery*, Vol. 11, No. 6, p. e1426, 2021.

[16] S. Zhang, Q. Deng, and Z. Ding, "Hyperspectral Image Segmentation based on Graph Processing over Multilayer Networks", *arXiv preprint arXiv:2111.15018*, 2021.

[17] Y. H. Li, X. Tan, W. Zhang, Q. B. Jiao, Y. X. Xu, H. Li, and Y. P. Fang, "Research and application of several key techniques in hyperspectral image preprocessing", *Frontiers in Plant Science*, Vol. 12, p. 627865, 2021.

[18] M. P. Uddin, M. A. Mamun, M. I. Afjal, and M. A. Hossain, "Information-theoretic feature selection with segmentation-based folded principal component analysis (PCA) for hyperspectral image classification", *International Journal of Remote Sensing*, Vol. 42, No. 1, pp. 286-321, 2021.

[19] X. Zhang, X. Jiang, J. Jiang, Y. Zhang, X. Liu, and Z. Cai, "Spectral–spatial and superpixelwise PCA for unsupervised feature extraction of hyperspectral imagery", *IEEE Transactions on Geoscience and Remote Sensing*, Vol. 60, pp. 1-10, 2021.

[20] P. D. Dao, K. Mantripragada, Y. He, and F. Z. Qureshi, "Improving hyperspectral image segmentation by applying inverse noise weighting and outlier removal for optimal scale selection", *ISPRS Journal of Photogrammetry and Remote Sensing*, Vol. 171, pp. 348-366, 2021.

[21] G. Aletti, A. Benfenati, and G. Naldi, "A semi-supervised reduced-space method for hyperspectral imaging segmentation", *Journal of Imaging*, Vol. 7, No. 12, 2021.

[22] P. Ajay, "Unsupervised Hyperspectral Microscopic Image Segmentation Using Deep Embedded Clustering Algorithm", *Scanning*, Vol. 2022, 2022.

[23] C. A. Hinojosa, F. Rojas, S. Castillo, and H. Arguello, "Hyperspectral image segmentation using 3D regularized subspace clustering model", *Journal of Applied Remote Sensing*, Vol. 15, No. 1, p. 016508, 2021.

[24] H. Sun, X. Zheng, and X. Lu, "A supervised segmentation network for hyperspectral image classification", *IEEE Transactions on Image Processing*, Vol. 30, pp. 2810-2825, 2021.

[25] M. P. Uddin, "Information-theoretic boundary selection with segmentation-based folded principal component analysis for hyperspectral image classification", *International Journal of Remote Sensing*, Vol. 42, No. 1, pp. 286-321, 2021.

[26] C. Mu, Z. Dong, and Y. Liu, "A Two-Branch Convolutional Neural Network Based on Multi-Spectral Entropy Rate Superpixel Segmentation for Hyperspectral Image Classification", *Remote Sensing*, Vol. 14, No. 7, 2022.

[27] J. Nalepa, M. Myller, M. Cwiek, L. Zak, T. Lakota, L. Tulczyjew, and M. Kawulok. "Towards on-board hyperspectral satellite image segmentation: understanding robustness of deep learning through simulating acquisition conditions", *Remote Sensing*, Vol. 13, No. 8, 2021.

[28] L. Wang, et al. "UNetFormer: A UNet-like transformer for efficient semantic segmentation of remote sensing urban scene imagery", *ISPRS Journal of Photogrammetry and Remote Sensing*, Vol. 190, pp. 196-214, 2022.

[29] C. Zhao, B. Qin, S. Feng, and W. Zhu, "Multiple superpixel graphs learning based on adaptive multiscale segmentation for hyperspectral image classification", *Remote Sensing*, Vol. 14, No. 3, 2022.

[30] S. Manju, and K. Helenprabha, "A structured support vector machine for hyperspectral satellite image segmentation and classification based on modified swarm optimization approach", *Journal of Ambient Intelligence and Humanized Computing*, Vol. 12, No. 3, pp. 3659-3668, 2021.

[31] Y. R. Fan, and T. Z. Huang, "Hyperspectral image restoration via superpixel segmentation of smooth band", *Neurocomputing*, Vol. 455, pp. 340-352, 2021.

[32] Siddiqa, Ayasha, R. Islam, and M. I. Afjal, "Spectral segmentation-based dimension reduction for hyperspectral image classification", *Journal of Spatial Science*, pp. 1-20, 2022.

[33] L. Ding, H. Tang, and L. Bruzzone, "LANet: Local attention embedding to improve the semantic segmentation of remote sensing images", *IEEE Trans. Geosci. Remote Sens.*, doi: 10.1109/TGRS.2020.2994150.

[34] G. Sun, "SpaSSA: Superpixelwise adaptive SSA for unsupervised spatial-spectral feature extraction in hyperspectral image", *IEEE Transactions on Cybernetics*, 2021.

[35] Y. Behroozi, and M. Yazdi, "Hyperspectral Image Denoising Based on Superpixel Segmentation Low-Rank Matrix Approximation and Total Variation", *Circuits, Systems, and Signal Processing*, Vol. 41, No. 6, pp. 3372-3396, 2022.